Petroleum Science 18 (2021) 1059–1068

Contents lists available at ScienceDirect

Petroleum Science

journal homepage: www.keaipublishing.com/en/journals/petroleum-science

Original Paper

# A physical model study of shale seismic responses and anisotropic inversion

Pin-Bo Ding [a, b], Fei Gong [a, b], Feng Zhang [a, b, *], Xiang-Yang Li [a, b]

[a] State Key Laboratory of Petroleum Resource and Prospecting, China University of Petroleum (Beijing), Beijing, 102249, China
[b] CNPC Key Laboratory of Geophysical Exploration, China University of Petroleum (Beijing), Beijing, 102249, China

ARTICLE INFO

*Article history:*
Received 18 November 2019
Accepted 26 January 2021
Available online 13 July 2021

Edited by Jie Hao

*Keywords:*
Physical model
Shale
Clay
AVO
Anisotropy

ABSTRACT

The seismic responses of the shale properties are critical for shale gas reservoir evaluation and production. It has been widely reported that the clay minerals have substantial influences on the seismic wave anisotropy and brittleness. Hence, knowing the seismic responses of the clay-rich shales and estimation of shale elastic properties are significant for the shale gas industry. A physical model containing two groups of shale blocks as the target formations is constructed in laboratory. The group S contains six shale blocks with different clay contents, and the group N contains six shale blocks with different porosity. The acquired 2D seismic data is used to analyze the seismic responses of two corresponding seismic lines. An anisotropic three-term inversion method is applied to one of the seismic inline to estimate the elastic properties the target shale blocks. The inversed attributes can be used to reveal the effects of shale clay contents. This study shows the substantial significance of using a physical model to observe the seismic responses of shale properties. The inversion results indicate that the anisotropic three-term inversion method could provide accurate results of elastic properties as well as the P- wave anisotropy parameter for shale formations.



## 1. Introduction

The exploration and production of shale gas resources have aroused both scientific and industrial interests in recent decades. Shales mostly represent strong vertical transverse isotropy caused by the intrinsic microstructure (Sayers, 1999; Vernik and Nur, 1992; Pan et al., 2020; Qian et al., 2020). The physical properties of the shales play important roles in seismic prospecting and inversion. The seismic responses of the shale properties still require more researches. Because of the intergrated result of many factors, such as the presence of clay and their contents, porosity et al., the seismic responses of shales are hard to be evaluated until now. Clays are one of the main minerals in Longmaxi marine shales in the Sichuan Basin in Southwest China (Wang et al., 2017; Zhou et al., 2019; Zhang, 2019; Gao et al., 2020). The clay contents could be up to 70% for continental shales in the Yanchang Formation in the Ordos Basin (Fu et al., 2015). Clay minerals are among the key factors for the high anisotropy of shales (Liu et al., 2019; Liu et al., 2019; Ding et al., 2019; Li et al., 2018), and make a substantial contribution to gas sorption and free gas storage (Yang et al., 2015; Gou and Xu, 2019). Because of the high degree of both heterogeneity and the anisotropy of shales, the effects of shale physical properties (composition, microstructure, clays) to seismic characteristics are hard to be evaluated (Guo et al., 2013; Zhang et al. 2017, 2018; Zhang, 2017). Based on the physical modeling method, synthetic shale samples were constructed to study the elastic properties affected by shale properties (Luan et al., 2016; Gong et al., 2018b; Xie et al., 2019).

Physical modeling is an important method to study the wavefield propagation in the complex unconventional reservoir. Previous studies have reported amount of researches on a complex medium such as, orthorhombic anisotropic (Cheadle et al., 1991), thin interbedding (Cooper et al., 2010), transversely isotropic media (Tapepalli et al., 1995; Ding et al., 2020), viscoelastic medium (Chen, 1996), complex structure imaging (Wu et al., 2014). Physical modeling can also be used to study the reservoir prediction and fluid identification (Wang et al., 2010), fracture prediction (Tatham et al., 1992), carbonate reservoir (Xu et al., 2016; Li et al., 2016), tight gas reservoir evaluation (Si et al., 2015).

* Corresponding author. State Key Laboratory of Petroleum Resource and Prospecting, China University of Petroleum (Beijing), Beijing, 102249, China.
*E-mail address:* zhangfeng@cup.edu.cn (F. Zhang).

https://doi.org/10.1016/j.petsci.2021.01.001

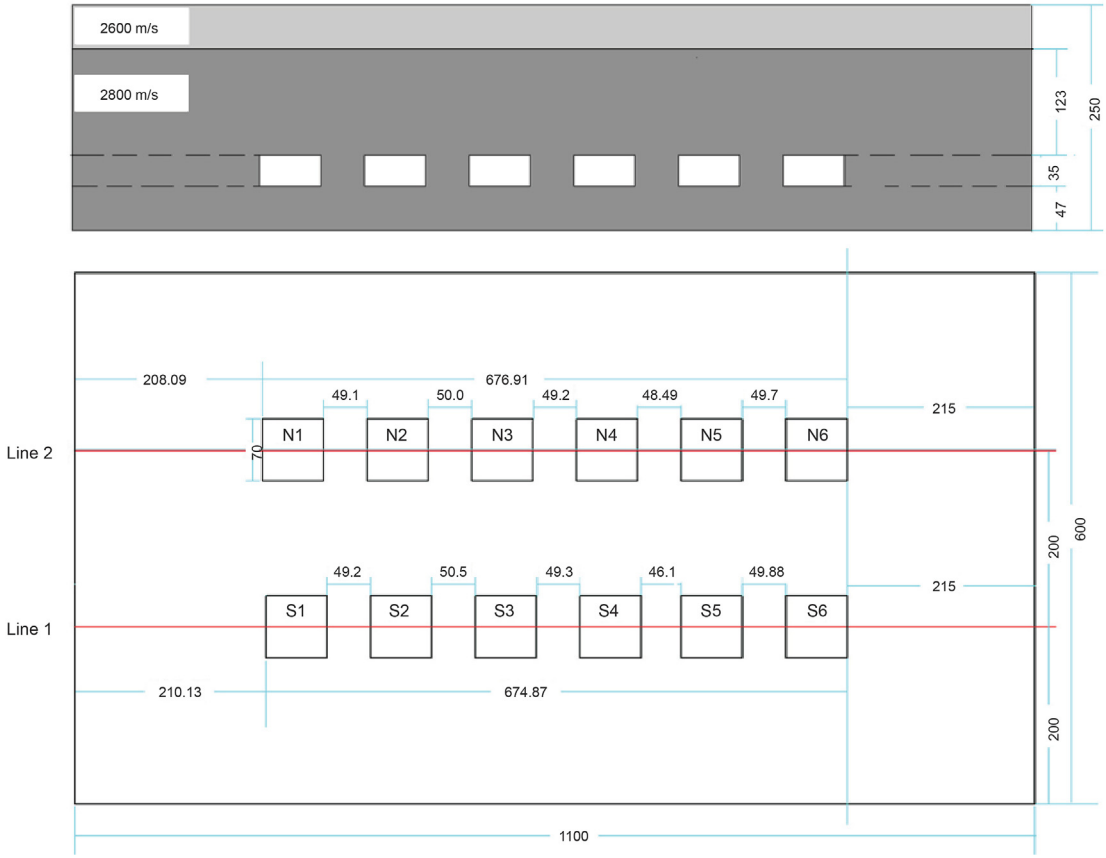


**Fig. 1.** The design of the physical model. The upper layer is isotropic and its P-wave velocity is 2600 m/s, while the lower layer is an isotropic layer containing two sets of shale blocks. The group N is shale blocks with porosity from 2.1% to 16.4%, group S is shale blocks with clay contents vary from 25% to 50%.

**Table 1**
Designed parameters of each layers in the physical model.

| Layer No. | density | Vp | Vs | Thickness |
|---|---|---|---|---|
| Water | 1 g/cc | 1480 m/s | 0 | 145 mm |
| 1 | 1.12 g/cc | 2600 m/s | 1200 m/s | 45 mm |
| 2 | 1.6 g/cc | 2800 m/s | 1400 m/s | 205 mm |

AVO inversion has been used to estimate elastic properties and to evaluate fracture properties of reservoir formations (Li et al., 2020). Because of the strongly intrinsic vertically transverse isotropy (VTI) of shale reservoir, seismic inversion for shale formation should involve anisotropy parameters (Zhang and Li, 2016; Liu et al., 2020; Yao et al., 2020). The anisotropic PP- wave approxi-

**Table 2a**
The construction parameters for group N shale blocks.

| Sample No. | Kaolinites | Quartz | Calcite | Kerogen | Glue | Compaction Pressure |
|---|---|---|---|---|---|---|
| N1 | 170 g | 280 g | 60 g | 40 g | 25 g | 20 MPa |
| N2 | 170 g | 280 g | 60 g | 40 g | 25 g | 40 MPa |
| N3 | 170 g | 280 g | 60 g | 40 g | 25 g | 60 MPa |
| N4 | 170 g | 280 g | 60 g | 40 g | 25 g | 80 MPa |
| N5 | 170 g | 280 g | 60 g | 40 g | 25 g | 100 MPa |
| N6 | 170 g | 280 g | 60 g | 40 g | 25 g | 120 MPa |

**Table 2b**
The construction parameters for group S shale blocks.

| Sample No. | Kaolinites | Quartz | Calcite | Kerogen | Glue | Compaction Pressure |
|---|---|---|---|---|---|---|
| S1 | 225 g | 150 g | 85 g | 40 g | 25 g | 200 MPa |
| S2 | 200 g | 175 g | 85 g | 40 g | 25 g | 200 MPa |
| S3 | 175 g | 200 g | 85 g | 40 g | 25 g | 200 MPa |
| S4 | 150 g | 225 g | 85 g | 40 g | 25 g | 200 MPa |
| S5 | 125 g | 250 g | 85 g | 40 g | 25 g | 200 MPa |
| S6 | 100 g | 275 g | 85 g | 40 g | 25 g | 200 MPa |

mations of reflection coefficient are used in many previous works of literatures (Castagna et al., 1993). Then this expression was modified to present an equation which is widely used in anisotropic AVO analysis (Rüger, 1997). Because of the difficulty of anisotropic inversion in VTI media, it was discussed that the effects of the two anisotropy parameters $\varepsilon$ and $\delta$ which was considered hard to be determined (Plessix and Bork, 2000). Lin and Thomsen (2013) developed a method to extract the anisotropy parameter $\delta$ based on the difference between the seismic amplitudes and synthetic amplitudes. Zhou et al. (2020) developed a nonlinear inversion for the VTI media. Zhang et al. (2019, 2020) used seismic amplitude inversion for VTI media to discriminate shale formation from surrounding formations.

We construct a physical model containing two groups of synthetic shale blocks with different properties to observe the corresponding seismic responses. The group S contains six shale blocks with different clay contents while group N contains six shale blocks with different porosity. Then we acquire 2D seismic data using the high-precision physical modeling acquisition system in CNPC Key Laboratory of Geophysical Exploration. We analyze the seismic responses in the stacked sections and the migrated sections of Line 1 and Line 2, corresponding to group S shales and group N shales, respectively. We use the three-term inversion method to estimate the elastic properties from the seismic data as well as the P- wave anisotropy parameter.

## 2. Construction of the physical models

### 2.1. Principles for seismic physical modeling

Seismic physical modeling, which is an important method to study the seismic exploration theory, is based on the similarity of the geometrical and physical parameters. The workflow of physical modeling includes three steps: 1) construct a physical model which has proper geometrical and physical parameters corresponding to the geological structure. 2) the seismic data acquisition which is simulated with an ultrasonic position system according to the predefined survey geometry. 3) seismic data processing and interpretation which can be used to analyze and solve various problems about seismic exploration.

In order to simulate the seismic wave propagation in the real field, several principles are considered for the physical modeling in the laboratory: 1) The corresponding parameters in the equations representing the modeling and original physical processes are similar. 2) The temporal and spatial similarity between the physical model and field. 3) The similarity between the initial and boundary conditions of the physical model and those in the field.

Because seismic wave propagation in field and ultrasonic wave have different frequency bands, hence the quantitative representations of the similar ratios are the scale factors. The scale factors for physical modeling are defined as the ratios between kinematic and dynamic parameters of the seismic wave in the field and those of the ultrasonic waves in the simulated physical model. The scale factor for velocity, spatial dimension, wave length and temporal sampling interval respectively is as follows,

$$\frac{V_r}{V_m} = \gamma_V \tag{1}$$

$$\frac{L_r}{L_m} = \gamma_L \tag{2}$$

$$\frac{\lambda_r}{\lambda_m} = \gamma_\lambda \tag{3}$$

$$\frac{\Delta T_r}{\Delta T_m} = \gamma_T \tag{4}$$

where $V_r$, $L_r$, $\lambda_r$, $\Delta T_r$ represent the velocity, spatial dimension, seismic wavelength and temporal sampling interval in the real field. $V_m$, $L_m$, $\lambda_m$ and $\Delta T_m$ represent those in physical modeling.

### 2.2. Model construction

To model the seismic responses of shales, we design a physical model with two layers. The size of physical model is 1100 mm × 600 mm × 250 mm, as shown in Fig. 1. The scale factor of the model/field for length, width, depth is 10000:1, i.e. 1 mm in the physical model presents 10m in the field. The physical model has two isotropic layers, shale formations are embedded in the second layer. In the second layer, two sets of shale blocks are embedded in the isotropic matrix. The parameters for the first layer and the second layer are shown in Table 1. We construct artificial shale blocks to simulate natural shales through the cold-pressing method, by applying the uniaxial effective pressure with no lateral train at room temperature (Gong et al., 2018a; Luan et al., 2016). We choose kaolinites, quartz, calcite and kerogen to construct the shale blocks. These minerals are also present as the major mineral components in natural shales. During the construction of shale blocks, a single variable is the porosity for Group N and clay content for Group S (as listed in Table 2). The powder is mixed in a ball mill to ensure a homogeneous composition, the mineral components by a certain weight proportion are listed in Table 2. The powder is then mixed with adhesives (An A/B double-component epoxy) to simulate the cementation of rocks. An amount of the mixture is placed in a mold and pressed each time. The sample is undergoing uniaxial effective stress until no lateral strain at ambient temperature for over 100 h, then removed from the mold. The mineral particles tent to be horizontally aligned due to the uniaxial effective pressure and induce vertical transverse isotropy which equivalent to the intrinsic anisotropy of shales.

For group N shale blocks, the porosities of each block are 2.1%, 3.8%, 4.7%, 7.8%, 11.5%, 16.4%. For group S shale blocks, the clay contents of each block are 25%, 30%, 35%, 40%, 45%, 50%. The porosities of the shale blocks are measured in the laboratory, and the clay contents of the shale blocks are calculated by weight from the mineral proportions in Table 2. The sizes of each shale blocks are all about 71mm × 71mm × 35mm. Fig. 1a gives a vertical view of the

**Table 3a**
Parameters of Group N shale blocks (Acquisition Line 2) used in the physical model.

| Sample No. | N-1 | N-2 | N-3 | N-4 | N-5 | N-6 |
|---|---|---|---|---|---|---|
| Porosity | 16.4% | 11.5% | 6.5% | 4.7% | 3.8% | 2.1% |
| $V_{P-X}$ | 2506 m/s | 2742 m/s | 2999 m/s | 3268 m/s | 3512 m/s | 3749 m/s |
| $V_{S-X}$ | 1564 m/s | 1736 m/s | 1943 m/s | 2120 m/s | 2311 m/s | 2496 m/s |
| $V_{P-Z}$ | 2200 m/s | 2350 m/s | 2503 m/s | 2672 m/s | 2830 m/s | 2992 m/s |
| $V_{S-Z}$ | 1389 m/s | 1512 m/s | 1655 m/s | 1780 m/s | 1898 m/s | 2023 m/s |
| Density | 2.48 g/cc | 2.52 g/cc | 2.54 g/cc | 2.56 g/cc | 2.61 g/cc | 2.63 g/cc |

**Table 3b**
Parameters of Group S shale blocks (Acquisition Line 1) used in the physical model.

| Sample No. | S-1 | S-2 | S-3 | S-4 | S-5 | S-6 |
|---|---|---|---|---|---|---|
| Clay content | 50% | 45% | 40% | 35% | 30% | 25% |
| $V_{P-X}$ | 3055 m/s | 3068 m/s | 3086 m/s | 3091 m/s | 3110 m/s | 3122 m/s |
| $V_{S-X}$ | 2059 m/s | 2072 m/s | 2099 m/s | 2105 m/s | 2133 m/s | 2142 m/s |
| $V_{P-Z}$ | 2568 m/s | 2585 m/s | 2650 m/s | 2690 m/s | 2732 m/s | 2776 m/s |
| $V_{S-Z}$ | 1766 m/s | 1790 m/s | 1837 m/s | 1878 m/s | 1917 m/s | 1950 m/s |
| Density | 2.48 g/cc | 2.52 g/cc | 2.54 g/cc | 2.56 g/cc | 2.61 g/cc | 2.63 g/cc |

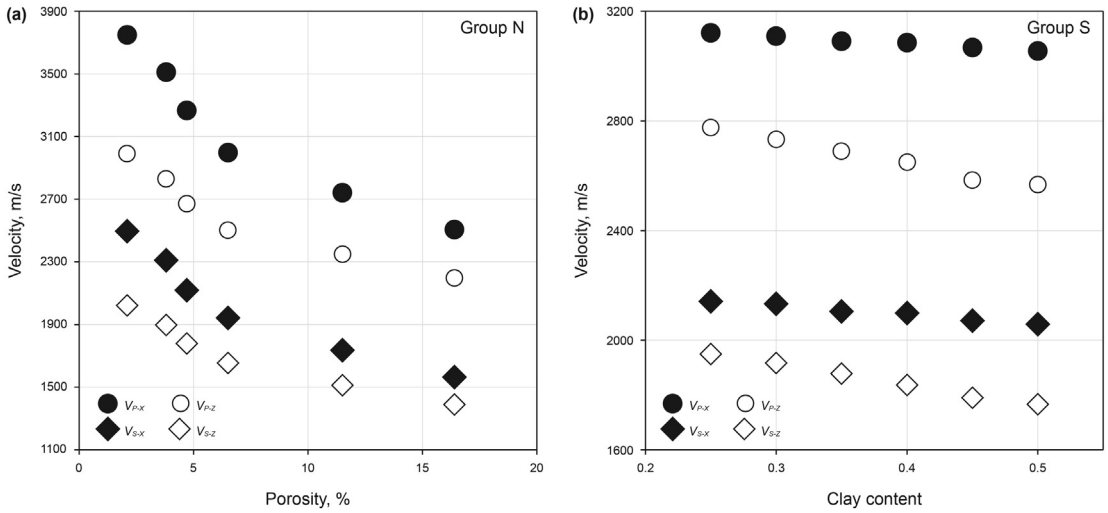


**Fig. 2.** The P- and S-wave velocities for group N shale blocks (porosity varies from 2.1% to 16.4%) and group S shale blocks (Clay contents vary from 25% to 50%). The $V_{P-X}$ and $V_{S-X}$ represent the measured velocities in bedding-parallel direction, $V_{P-Z}$ and $V_{S-Z}$ represent the measured velocities in bedding-normal direction.

two sets of shale blocks distribution within the second layer, the blocks are embedded in the second layer at the same depth and aligned as N1 − N6 which have various porosity and S1 − S6 with various clay contents. Fig. 1b give a top-down view of the second layer, the group N shale blocks and group S shale blocks aligned along the X-direction. The shale physical model is constructed layer by layer, the second layer was constructed in a mold and two sets of shale blocks were embedded in the physical model during the construction of this layer. The model was left for consolidation for 7 days, then the first layer was constructed above the consolidated second layer. Then the physical model was left for two weeks for final consolidation.

### 2.3. Analyze the shale anisotropy

We use ultrasonic testing devices to measure the elastic velocities of each shale blocks, the dominant frequency of the ultrasonic transducers used in the ultrasonic measurement is 0.5 MHz. The

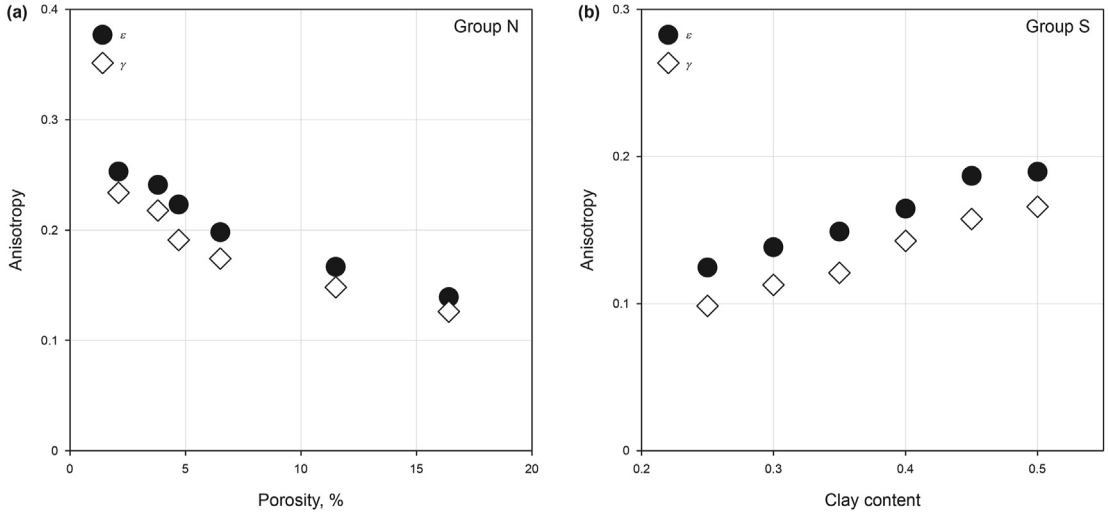


**Fig. 3.** The P- and S-wave anisotropy for group N shale blocks (porosity varies from 2.1% to 16.4%) and group S shale blocks (Clay contents vary from 25% to 50%). The P- and S-wave anisotropy is provided by the measured velocities in bedding-normal direction and bedding-parallel direction. ε and γ are the anisotropic parameters defined by (Thomsen, 1986).

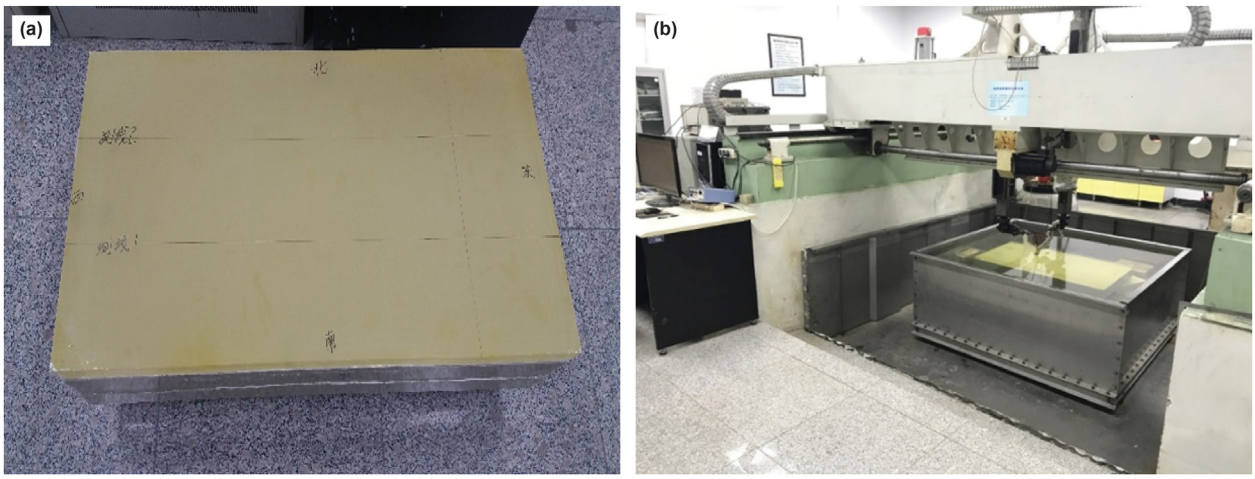


**Fig. 4.** The constructed shale physical model (a) and the acquisition system (b).

**Table 4**
The 2D acquisition geometry parameters.

| | In model scale | In field scale |
|---|---|---|
| Number of traces | 184 | 184 |
| Number of shots | 500 | 500 |
| Minimum offset | 16 mm | 160 m |
| Maxim offset | 199 mm | 1990 m |
| Trace interval | 1 mm | 10 m |
| Shot interval | 2 mm | 20 m |
| Time interval | 0.1 us | 1 ms |
| Number of time samples | 4096 | 4096 |

density and velocities of each block are shown in Table 3. Fig. 2a shows the P- and S-wave velocities for Group N, velocities decrease sharply with the increasing porosity for both P- and S-wave. This phenomenon is more apparent when porosity is lower than 10%. Fig. 2b shows the P- and S-wave velocities for Group S, velocities slightly decrease as the clay content increase from 25% to 50%. This indicates that P- and S- wave velocities are more sensitive to porosity than clay contents. However, the difference of velocities between bedding-normal and bedding-parallel direction shows a significant increase in Fig. 2b. We calculate the anisotropy based on the measured velocities in different direction of each blocks. The anisotropy parameters for P- and S-wave are defined by (Thomsen, 1986) as:

$$\varepsilon \approx \frac{V_P(90^\circ) - V_P(0^\circ)}{V_P(0^\circ)} = \frac{V_{P-X} - V_{P-Z}}{V_{P-Z}} \tag{5}$$

and

$$\gamma \approx \frac{V_{SH}(90^\circ) - V_{SH}(0^\circ)}{V_{SH}(0^\circ)} = \frac{V_{S-X} - V_{S-Z}}{V_{S-Z}} \tag{6}$$

where $V_P(90^\circ)$ and $V_P(0^\circ)$ are the P- wave velocity in bedding-parallel $V_{P-X}$ and bedding-normal $V_{P-Z}$ direction, $V_{SH}(90^\circ)$ and $V_{SH}(0^\circ)$ are the SH- wave velocities in bedding-parallel $V_{S-X}$ and bedding-normal $V_{S-Z}$ direction. Fig. 3 shows the anisotropy parameters $\varepsilon$ and $\gamma$ of group N and group S. Fig. 3a shows the P- and S-wave anisotropy decrease as the porosity increase from 2.1% to 16.4%, while Fig. 3b shows the anisotropy parameters increase with the increasing clay content. Comparatively, P- and S-wave anisotropy is very sensitive to the clay content as shown in Fig. 3b.

## 3. Seismic data acquisition and seismic response analysis

### 3.1. Physical modeling data acquisition

The shale physical model is soaked in a water tank inside the acquisition system for 1 month before the data acquisition, the acquisition system should be ensured to remain stable that no water flow and disturbance in the water tank (as shown in Fig. 4). The thickness of the water is 145 mm (i.e. 1450 m in the field scale), the parameters of the water layer are also shown in Table 1. We designed an acquisition geometry for the shale physical model. The dominant frequency of the transducers used in 2D reflection data acquisition is 0.5 MHz, the number of shots is 500 and the number of traces is 184, the minimum offset is 16 mm (i.e. 160 m in the field scale), the trace interval is 1 mm (i.e. 10 m in the field scale), the shot interval is 2 mm (i.e. 20 m in the field scale), the time sample interval is 0.1us (i.e. 1 ms in the field scale), and the number of time samples is 4096. Note that the scale factor is 10000:1, i.e. 1 mm in physical model presents 10 m in the field, 1 us in physical modeling presents 10 ms in field data. The geometry parameters for both Line 1 and Line 2 are shown in Table 4. Acquisition Line 1 is a seismic profile acquired for group S with different clay contents, while acquisition Line 2 was that for group N with different porosity. Because the noise in physical modeling is less in physical modeling, the signal-to-noise ratio is high. The reflection events of the strata and the shale blocks could be seen on the profile clearly.

### 3.2. Seismic responses analysis of the shale properties

The acquired seismic data is processed to observe the seismic responses of the shale blocks with different parameters. Figs. 5a and 6a show the stack sections for Line 1 and Line 2 respectively. The reflection of the top and bottom interfaces of the shale blocks are between 3200 ms and 3600 ms. The left and right sides of the stack sections in Figs. 5a and 6a show the waves reflected by the boundaries of the physical model, this boundary effects have no substantial influence on the refection events of the shale blocks. There are several refection events on the top of the section between 2800 ms and 3200 ms, these are caused by the multiple reflection events from the interface between the water layer and the first layer, and also the multiple reflection events from the interface between the first layer and the second layer. The stack sections shown in Figs. 5a and 6a present a series of diffraction waves on the top and bottom refection events of the shale blocks.

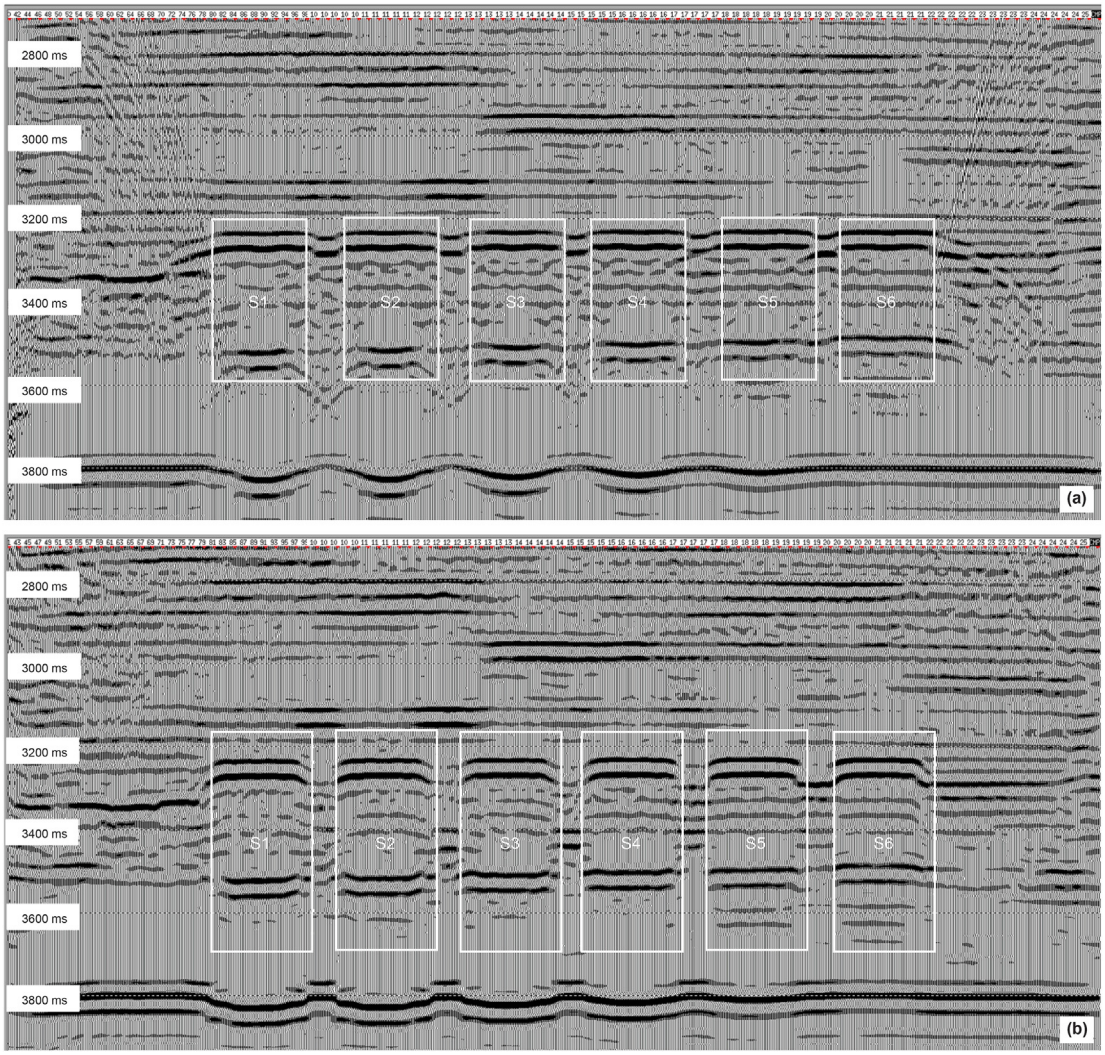


**Fig. 5.** The stack section (a) and the migration section (b) of Line 1 (group S with different clay contents).

Figs. 5b and 6b shows the prestack time migration sections of Line 1 and Line 2 respectively, the effects of the diffraction waves of each block are removed after seismic migration. Also, the influences of the boundary effects of the physical model are reduced after seismic migration as shown in Figs. 5b and 6b. Because of the effects of shale blocks, the reflection evens of the bottom of the physical model present curved at about 3800 ms in the stack section shown in Figs. 5 and 6. Comparatively, the shale blocks with higher clay contents (i.e. blocks S1 and S2) have a more apparent influence on the bottom refection events than shale blocks with lower clay contents (i.e. blocks S5 and S6). Because the blocks with high clay contents have lower seismic velocity, especially in the vertical direction, the reflection events bellow the blocks S1 and S2 are more apparently curved. For Line 2, the block N1 and N2 with much higher porosity and lower seismic velocity, hence have a more apparent influence on the bottom refection of the physical model.

Comparing Fig. 6 with Fig. 5, Line 2 presents more substantial effects to the bottom reflection events than Line 1. Meanwhile, the seismic reflection events appear to be more significantly attenuated in Line 2 than Line1. These phenomena deduce that the seismic responses of the shale blocks are more sensitive to the porosity changes (from 2.1% to 16.4) than the clay content variation (from 25% to 50%). Figs. 2 and 3 show that the variation of velocity and anisotropy caused by porosity is more substantial than that by clay content. Hence the reflection responses caused by porosity variation in Fig. 6 are more apparent than that in Fig. 5. Nevertheless, the porosity of nature shales would be not as high as N1 and N2 because of the porosity variation are commonly low.

## 4. Anisotropic inversion based on a modified AVO equations

Shale blocks are observed as VTI media. Thus an anisotropic AVO inversion algorithm based on an modified approximation of the PP-wave reflection coefficient Besides, the P-wave anisotropy parameter $\varepsilon$ could be also estimated according to the inverted anisotropic P-wave velocity.

### *4.1. AVO equation in the transversely isotropic media with vertical axis of symmetry*

The P–P wave reflection coefficient for a VTI media for the $i$-th planar interface separating the $i$-th and the $i$+1-th VTI layers is given by (Zhang et al., 2019) as

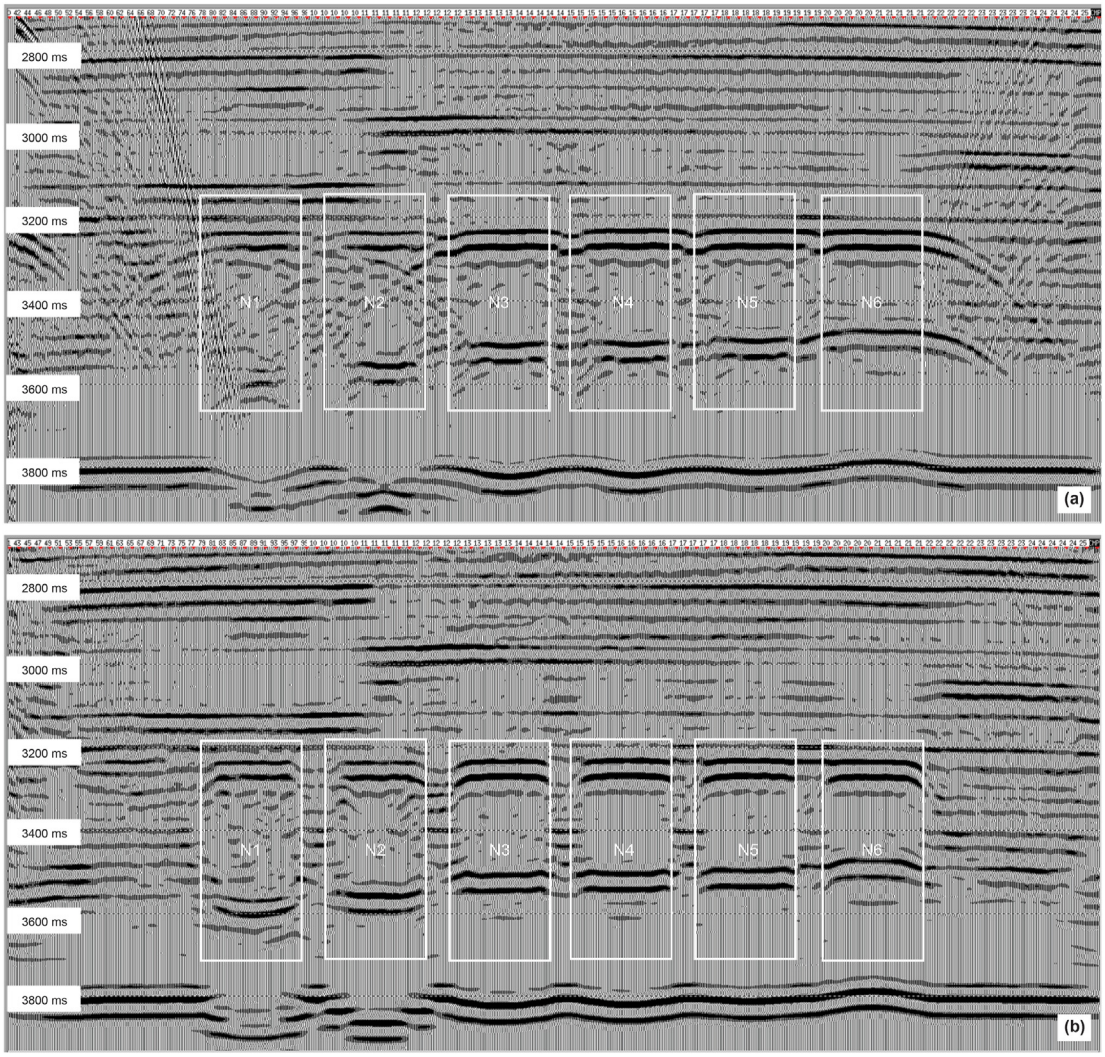


**Fig. 6.** The stack section (a) and the migration section (b) of Line 2 (group N with different porosity).

$$R_{VTI}(\theta) = \frac{1}{2}\ln\left(\frac{A_{i+1}}{A_i}\right) - \frac{1}{2}K\sin^2(\theta)\ln\left(\frac{B_{i+1}}{B_i}\right) + \frac{1}{2}\tan^2(\theta)\ln\left(\frac{C_{i+1}}{C_i}\right) \tag{7}$$

where $A = \rho V_{P0}$ represents the acoustic impedance, $B = \rho V_{S0}^2 e^{\sigma}_{\delta}$ is the weighted shear modulus of anisotropy $\sigma = (V_{S0}/V_{P0})^2(\varepsilon - \delta)$ is the effective parameter), and $C = V_{P0}e^{\varepsilon}$ represents the horizontal P-wave velocity $V_{P90} \approx V_{P0}(1+\varepsilon)$,$\rho$ is the density, $V_{P0}$ and $V_{S0}$ are the P- and S-wave vertical velocity of the media. $\theta$ is the angle of the incidence. A model vector that consisting of the three model parameters $\boldsymbol{m} = [\boldsymbol{A}, \boldsymbol{B}, \boldsymbol{C}]^{\mathrm{T}}$ can be solved by using an iterative inversion scheme

$$\boldsymbol{m} = \boldsymbol{m}_{\mathrm{prior}} + \left(\boldsymbol{G}^{\mathrm{T}}\boldsymbol{G} + \mu\boldsymbol{C}_{\mathrm{m}}^{-1}\right)^{-1}\boldsymbol{G}^{\mathrm{T}}\Delta\boldsymbol{d} \tag{8}$$

where $\boldsymbol{m}_{\mathrm{prior}}$ is the prior model parameter vector, $\boldsymbol{G}$ is the mapping operator from model to data, and it includes the effect of incident angles and wavelets, and $\Delta\boldsymbol{d}$ is the data residual, $\mu$ proportional is the trade-off parameter of the regularization term.

Three attributes ($A$, $B$, $C$) can be directly inverted by using above method. Then the independent anisotropy parameter ε, which reflect the anisotropy magnitude of the media, can be recovered from the inverted parameter $C$ by using two steps: (1) simultaneous inversion using isotropic AVO equation for the vertical P-wave phase velocity ($V_{P0}$) using small-angle reflection seismic data; (2) the anisotropy parameter ε is estimated using inverted $V_{P0}$ and the attribute $C = V_{P0}e^{\varepsilon}$ as $\ln\left(\frac{C}{V_{P0}^{\mathrm{est}}}\right)$.

### 4.2. Inversion results of shale physical modeling data

We apply the three-term inversion method on Line 1 that has shale blocks with different clay contents. Fig. 7 shows the results of terms $A$, $B$ and $C$, respectively. Also, the isotropic inversion result is shown in Fig. 8. Fig. 7a shows the acoustic impedance for the shale blocks with different clay contents, the acoustic impedance is apparently affected by the clay content because the inversion results for S1 and S2 blocks with low clay contents are comparatively higher than S5 and S6 with high clay contents. The shear modulus results inversed from term $B$ shown in Fig. 7b seams not significantly affected by the various clay contents. The inverted horizontal P-wave velocity determined by the term $C$ shown in Fig. 7c is not substantially affected because the $V_{P90}$ is less affected by the clay contents. Fig. 8 shows the isotropic inversion result and represents

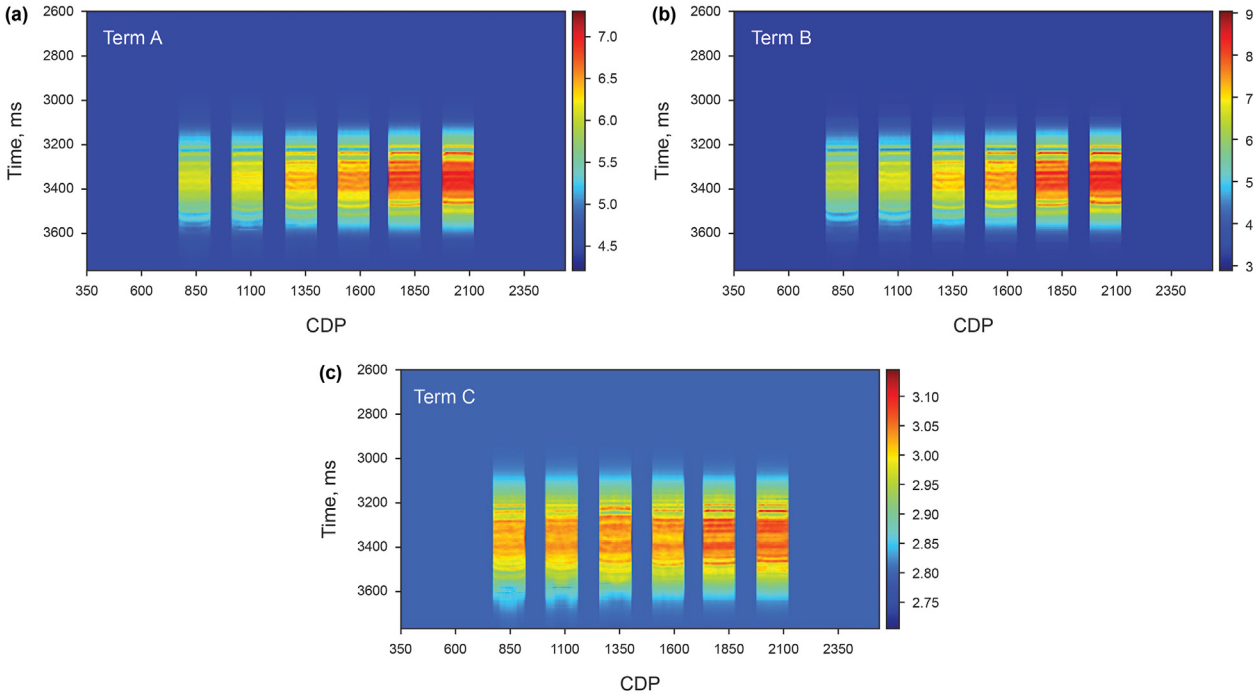


**Fig. 7.** The results of three-term inversion for term *A* (a) and term *B* (b) and term *C* (c) for Line 1 (group S with different clay contents).

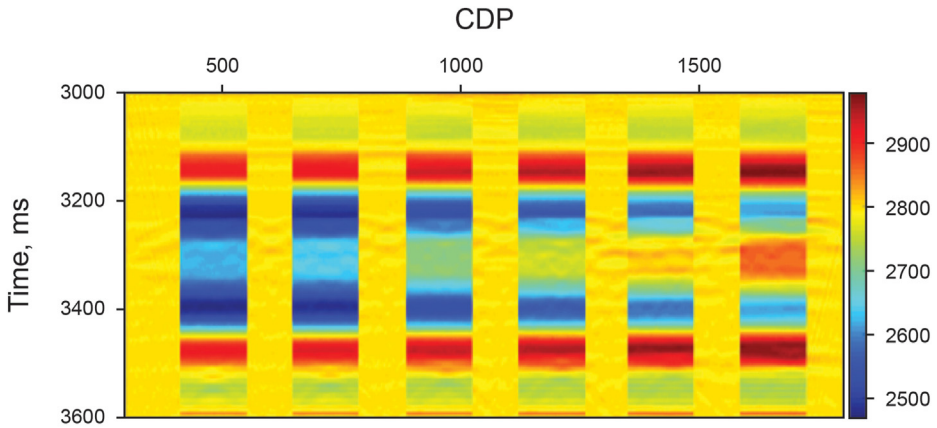


**Fig. 8.** The isotropic inversion results for Line 1 (group S with different clay contents).

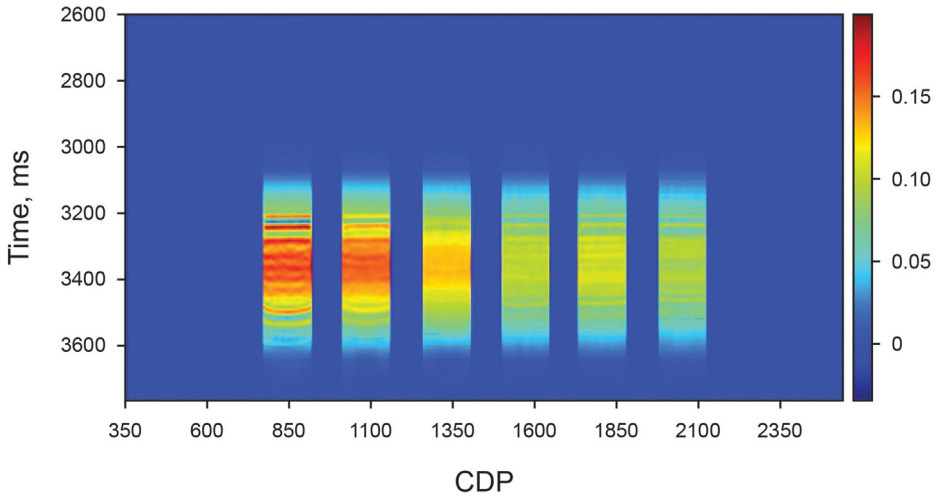


**Fig. 9.** The inversed P-wave anisotropy parameter for Line 1 (group S with different clay contents).

less accuracy than the three-term inversion results shown in Fig. 7. As introduced above, the three-term inversion could also extract the P-wave anisotropy parameter ε according to the inverted anisotropic P-wave velocity. As shown in Fig. 9, the estimated P-wave anisotropy parameter ε is high in block S5 and S6 with high clay contents, and low in blocks S5 and S6 with low clay contents. This inversion results highly agree with the measured P-wave anisotropy shown in Fig. 3. All these figures indicate that the three-term inversion method could accurately inverse the elastic parameters of the shales as well as the P-wave anisotropy parameter.

Because the physical modeling provides the controlled parameters (e.g. the geometrical and physical properties shown in Tables 1–4), hence the responses of the shales can be quantitatively related to the variation of the parameters. The inversion results also can be verified by comparing to the known parameters of the physical model. The comparison between the isotropic inversion in Fig. 7 and anisotropic inversion results indicate that the three-term inversion can provide quantitatively better results for shale properties analysis during the shale rock sweet-point evaluation.

## 5. Conclusions

Physical modeling is an effective method to investigate the seismic responses of varied reservoir. In this study, we construct a physical model with two groups of shale blocks and acquired 2D seismic data. The seismic responses of group S (shale blocks with different clay contents) and group N (shale blocks with different porosity) are analyzed. The results show the various clay contents and porosity have a substantial influence on the seismic reflection. Then we use the three-term inversion method to estimate the elastic properties as well as the P-wave anisotropy parameter. The three-term inversion method could accurately invert the elastic parameters of the shales as well as the P-wave anisotropy parameter.

## Acknowledgements

This research is supported by the National Natural Science Fund Projects (U19B6003), Strategic Cooperation Technology Projects of CNPC and CUPB (ZLZX2020-03) and the Science Foundation of China University of Petroleum (Beijing) (2462020YXZZ008).

## References

Castagna, J.P., Spratt, R.S., Goins, N.R., Fitch, T.J., Dey-Sarkar, S.K., Svatek, S.V., et al., 1993. Principles. In: Castagna, J.P., Backus, M.M. (Eds.), Offset-Dependent Reflectivity—Theory and Practice of AVO Analysis. Society of Exploration Geophysicists.

Cheadle, S.P., Brown, R.J., Lawton, D.C., 1991. Orthorhombic anisotropy: a physical seismic modeling study. Geophysics 56 (10), 1603–1613. https://doi.org/10.1190/1.1442971.

Chen, G., 1996. Comparison of 2-D numerical viscoelastic waveform modeling with ultrasonic physical modeling. Geophysics 61 (3), 862–871. https://doi.org/10.1190/1.1444011.

Cooper, J.K., Lawton, D.C., Margrave, G.F., 2010. The wedge model revisited: a physical modeling experiment. Geophysics 75 (2), T15–T21. https://doi.org/10.1190/1.3309641.

Ding, P., Wang, D., Di, G., Li, X., 2019. Investigation of the effects of fracture orientation and saturation on the Vp/Vs ratio and their implications. Rock Mech. Rock Eng. 52 (9), 3293–3304. https://doi.org/10.1007/s00603-019-01770-3.

Ding, P., Wang, D., Li, X.-Y., 2020. An experimental study on scale-dependent velocity and anisotropy in fractured media based on artificial rocks with controlled fracture geometries. Rock Mech. Rock Eng. 53 (7), 3149–3159. https://doi.org/10.1007/s00603-020-02095-2.

Fu, H., Wang, X., Zhang, L., Gao, R., Li, Z., Zhu, X., et al., 2015. Geological controls on artificial fracture networks in continental shale and its fracability evaluation: a case study in the Yanchang Formation, Ordos Basin, China. J. Nat. Gas Sci. Eng. 26, 1285–1293. https://doi.org/10.1016/j.jngse.2015.08.034.

Gao, Z., Fan, Y., Xuan, Q., Zheng, G., 2020. A review of shale pore structure evolution characteristics with increasing thermal maturities. Advances in Geo-Energy Research 4 (3), 247–259.

Gong, F., Di, B., Wei, J., Ding, P., Li, H., Li, D., 2018a. Experimental investigation of the effects of clay content and compaction stress on the elastic properties and anisotropy of dry and saturated synthetic shale. Geophysics 83 (5), C195–C208. https://doi.org/10.1190/geo2017-0555.1.

Gong, F., Di, B., Wei, J., Ding, P., Shuai, D., 2018b. Dynamic mechanical properties and anisotropy of synthetic shales with different clay minerals under confining pressure. Geophys. J. Int. 212 (3), 2003–2015. https://doi.org/10.1093/gji/ggx537.

Gou, Q., Xu, S., 2019. Quantitative evaluation of free gas and adsorbed gas content of Wufeng-Longmaxi shales in the Jiaoshiba area, Sichuan Basin, China. Advances in Geo-Energy Research 3 (3), 258–267.

Guo, Z., Li, X., Liu, C., Feng, X., Shen, Y., 2013. A shale rock physics model for analysis of brittleness index, mineralogy and porosity in the Barnett Shale. J. Geophys. Eng. 10 (2), 25006.

Li, L., Zhang, J.J., Pan, X.P., Zhang, G.Z., 2020. Azimuthal elastic impedance-based Fourier coefficient variation with angle inversion for fracture weakness. Petrol. Sci. 17 (1), 86–104. https://doi.org/10.1007/s12182-019-00405-0.

Li, Q., Di, B., Wei, J., Yuan, S., Si, W., 2016. The identification of multi-cave combinations in carbonate reservoirs based on sparsity constraint inverse spectral decomposition. J. Geophys. Eng. 13 (6), 940–952.

Li, X., Lei, X., Li, Q., 2018. Response of velocity anisotropy of shale under isotropic and anisotropic stress fields. Rock Mech. Rock Eng. 51 (3), 695–711. https://doi.org/10.1007/s00603-017-1356-2.

Lin, R., Thomsen, L., 2013. Extracting Polar Anisotropy Parameters from Seismic Data and Well Logs. SEG Technical Program Expanded Abstracts, pp. 310–314.

Liu, K., Ostadhassan, M., 2019. The impact of pore size distribution data presentation format on pore structure interpretation of shales. Advances in Geo-Energy Research 3 (2), 187–197.

Liu, S.Y., Zhang, Y.Z., Li, C., Sun, W.Y., Fang, G., Liu, G.C., 2020. Automatic estimation of traveltime parameters in VTI media using similarity-weighted clustering. Petrol. Sci. 17 (2), 363–375. https://doi.org/10.1007/s12182-019-00423-y.

Liu, Z., Zhang, F., Li, X., 2019. Elastic anisotropy and its influencing factors in organic-rich marine shale of southern China. Sci. China Earth Sci. 62 (11), 1805–1818. https://doi.org/10.1007/s11430-019-9449-7.

Luan, X., Di, B., Wei, J., Zhao, J., Li, X., 2016. Creation of synthetic samples for physical modelling of natural shale. Geophys. Prospect. 64 (4), 898–914.

Pan, X.P., Zhang, G.Z., Chen, J.J., 2020. The construction of shale rock physics model and brittleness prediction for high-porosity shale gas-bearing reservoir. Petrol. Sci. 17 (3), 658–670. https://doi.org/10.1007/s12182-020-00432-2.

Plessix, R.E., Bork, J., 2000. Quantitative estimate of VTI parameters from AVA responses. Geophys. Prospect. 48 (1), 87–108. https://doi.org/10.1046/j.1365-2478.2000.00175.x.

Qian, K.R., Liu, T., Liu, J.Z., Liu, X.W., He, Z.L., Jiang, D.J., 2020. Construction of a novel brittleness index equation and analysis of anisotropic brittleness characteristics for unconventional shale formations. Petrol. Sci. 17 (1), 70–85. https://doi.org/10.1007/s12182-019-00372-6.

Rüger, A., 1997. P-wave reflection coefficients for transversely isotropic models with vertical and horizontal axis of symmetry. Geophysics 62 (3), 713–722. https://doi.org/10.1190/1.1444181.

Sayers, C.M., 1999. Stress-dependent seismic anisotropy of shales. Geophysics 64 (1), 93–98.

Si, W., Di, B., Wei, J., 2015. Seismic response variation of tight gas sand for uniform and patchy saturation patterns. J. Appl. Geophys. 116, 167–172. https://doi.org/10.1016/j.jappgeo.2015.03.010.

Tapepalli, S.V., Tatham, R.H., Ebrom, D.A., McDonald, J.A., 1995. AVO in Transversely Isotropic Media: A Physical Modeling Experiment. SEG Technical Program Expanded Abstracts, pp. 596–599, 1995.

Tatham, R., Matthews, M., Sekharan, K., Wade, C., Liro, L., 1992. A physical model study of shear-wave splitting and fracture intensity. Geophysics 57 (4), 647–652. https://doi.org/10.1190/1.1443278.

Thomsen, L., 1986. Weak elastic anisotropy. Geophysics 51 (10), 1954–1966. https://doi.org/10.1190/1.1442051.

Vernik, L., Nur, A., 1992. Ultrasonic velocity and anisotropy of hydrocarbon source rocks. Geophysics 57 (5), 727–735. https://doi.org/10.1190/1.1443286.

Wang, L., Fu, Y., Li, J., Sima, L., Wu, Q., Jin, W., et al., 2017. Experimental study on the wettability of Longmaxi gas shale from Jiaoshiba gas field, Sichuan Basin, China. J. Petrol. Sci. Eng. 151, 488–495. https://doi.org/10.1016/j.petrol.2017.01.036.

Wang, S., Li, X.-Y., Di, B., Booth, D., 2010. Reservoir fluid substitution effects on seismic profile interpretation: a physical modeling experiment. Geophys. Res. Lett. 37 (10). https://doi.org/10.1029/2010gl043090.

Wu, M.S., Di, B.R., Wei, J.X., Liang, X.H., Zhou, Y., Liu, Y.M., et al., 2014. Large-scale complex physical modeling and precision analysis. Appl. Geophys. 11 (2), 245–251. https://doi.org/10.1007/s11770-014-0434-4.

Xie, J., Cao, J., Schmitt, D.R., Di, B., Xiao, L., Wang, X., et al., 2019. Effects of kerogen content on elastic properties-based on artificial organic-rich shale (AORS). J Geophys Res Solid Earth 124 (12), 12660–12678. https://doi.org/10.1029/2019jb017595.

Xu, C., Di, B., Wei, J., 2016. A physical modeling study of seismic features of karst cave reservoirs in the Tarim Basin, China. Geophysics 81 (1), B31–B41. https://doi.org/10.1190/geo2014-0548.1.

Yang, F., Ning, Z., Zhang, R., Zhao, H., Krooss, B.M., 2015. Investigations on the methane sorption capacity of marine shales from Sichuan Basin, China. Int. J. Coal Geol. 146, 104–117. https://doi.org/10.1016/j.coal.2015.05.009.

Yao, G., Wu, D., Wang, S.X., 2020. A review on reflection-waveform inversion. Petrol. Sci. 17 (2), 334–351. https://doi.org/10.1007/s12182-020-00431-3.

Zhang, F., 2017. Estimation of anisotropy parameters for shales based on an improved rock physics model, part 2: case study. J. Geophys. Eng. 14 (2), 238–254. https://doi.org/10.1088/1742-2140/aa5afa.
Zhang, F., Li, X.-Y., 2016. Exact elastic impedance matrices for transversely isotropic medium. Geophysics 81 (2), C1–C15. https://doi.org/10.1190/geo2015-0163.1.
Zhang, F., Li, X.-Y., Qian, K., 2017. Estimation of anisotropy parameters for shale based on an improved rock physics model, part 1: theory. J. Geophys. Eng. 14 (1), 143–158.
Zhang, F., Wang, L., Li, X.-Y., 2020. Characterization of a shale-gas reservoir based on a seismic AVO inversion for VTI media and quantitative seismic interpretation. Interpretation 8 (1), SA11–SA23. https://doi.org/10.1190/int-2019-0050.1.
Zhang, F., Zhang, T., Li, X.-Y., 2019. Seismic amplitude inversion for the transversely isotropic media with vertical axis of symmetry. Geophys. Prospect. 67 (9), 2368–2385. https://doi.org/10.1111/1365-2478.12842.
Zhang, F., 2019. A modified rock physics model of overmature organic-rich shale: application to anisotropy parameter prediction from well logs. J. Geophys. Eng. 16 (1), 92–104. https://doi.org/10.1093/jge/gxy008.
Zhang, Y.Y., Jin, Z.J., Chen, Y.Q., Liu, X.W., Han, L., Jin, W.J., 2018. Pre-stack seismic density inversion in marine shale reservoirs in the southern Jiaoshiba area, Sichuan Basin, China. Petrol. Sci. 15 (3), 484–497. https://doi.org/10.1007/s12182-018-0242-1.
Zhou, H.T., Li, D.Y., Liu, X.T., Du, Y.S., Gong, W., 2019. Sweet spot prediction in tight sandstone reservoir based on well-bore rock physical simulation. Petrol. Sci. 16 (6), 1285–1300. https://doi.org/10.1007/s12182-019-00393-1.
Zhou, L., Chen, Z.C., Li, J.Y., Chen, X.H., Liu, X.Y., Liao, J.P., 2020. Nonlinear amplitude versus angle inversion for transversely isotropic media with vertical symmetry axis using new weak anisotropy approximation equations. Petrol. Sci. 17 (3), 628–644. https://doi.org/10.1007/s12182-020-00445-x.